

Modeling Humidity Impact on PDIV for Turn-to-Turn Insulation of Inverter-Fed Motors at Different Temperatures

H. Naderiallaf, Y. Ji, P. Giangrande and M. Galea

Abstract— This paper models the partial discharge inception voltage (PDIV) as a function of ambient humidity (H) at various temperatures (T_s) using Schumann's streamer inception criterion (SCSIC) for turn-to-turn insulation, which is the most vulnerable part in inverter-fed motors' insulation system. The Schumann constant (i.e., the natural logarithm of the critical electron number defining the Townsend-to-streamer discharge transition, K) varies with H , showing distinct patterns at low and high T_s . The K equations are derived across a wide range of relative humidity (RH) levels (20%, 30%, 40%, 50%, 60%, 70%, 80%, and 90%) at four T_s (25°C, 40°C, 60°C, and 90°C). These equations can be used in finite element analysis software to predict PDIV under varying H with outstanding accuracy. Additionally, a novel approach is presented for partial discharge (PD) phenomenology under H variations at different T_s using SCSIC-derived streamer inception parameters (SIPs): critical field line length (CFL), air effective ionization coefficient (α_{eff}), partial discharge (PD) inception field (E_{inc}) and firing voltage (V_{firing}). Notably, at high T_s (e.g., 90°C), a transition phase emerges concerning RH, leading to significant SIP changes due to the disappearance of a critical region (CritR) in α_{eff} at specific electric field intensities. The developed humidity-dependent PDIV model supports insulation designers in achieving PD-free designs that account for H variations and sheds light on SIPs variations concerning H changes.

Index Terms— Electric machines, finite element analysis, humidity, insulation, modeling, partial discharges, reliability.

NOMENCLATURE

AEA	All-electric aircraft
AH	Absolute humidity
B10	10 th percentile
CFL	Critical field line
CFL	Critical field line length
CritR	Critical region
DEA	Dissociative electron attachment
E_{inc}	Partial discharge inception field

EV	Electric vehicle
FEM	Finite element method
FL	Field line
FLL	Field line length
H	Ambient humidity
HEV	Hybrid electric vehicle
HFCT	Ferrite-core high-frequency current transformer
HV	High voltage
K	Schumann constant
MEA	More electric aircraft
PD	Partial discharge
PDIV	Partial discharge inception voltage
RH	Relative humidity
SCSIC	Schumann's streamer inception criterion
SIP	Streamer inception parameter
T	Temperature
$\tan\delta$	Dielectric dissipation factor
TPs	Twisted pairs
V_{firing}	Firing voltage
α	Ionization coefficient of air
α_{eff}	Effective ionization coefficient of air
ϵ_r	Relative permittivity of solid insulation
ϵ_{rw}	Water relative permittivity
η	Attachment coefficient of air

I. INTRODUCTION

BY 2050, ambitious environmental targets have been set: reducing CO₂ emissions by 75%, nitrogen oxide emissions by 90%, and noise emissions by 65% [1]. EVs, HEVs, MEA, and AEA are globally recognized for their significant carbon footprint reduction. Central in the electrification process is the electric drive, comprising the battery, inverter, and traction motor. Notably, current trends encompass the implementation of inverters featuring elevated DC bus voltages (ranging from 600 to 1000 V) and heightened dV/dt to enhance energy efficiency and power density. Nonetheless, this evolution imposes significant electrical

Yatai Ji is with the Key Laboratory of More Electric Aircraft Technology of Zhejiang Province, University of Nottingham Ningbo, China, Ningbo, China. (e-mail: yatai.ji@nottingham.edu.cn).

Paolo Giangrande is with the Department of Engineering and Applied Sciences, University of Bergamo, Dalmine, Italy (e-mail: paolo.giangrande@unibg.it).

Michael Galea is with the Department of Industrial Electrical Power Conversion, University of Malta, Msida, Malta (e-mail: michael.d.galea@um.edu.mt).

This paper was submitted for review in October 2023. This work was partially supported by Project AIMS1, financed by the Malta Council for Science & Technology, for and on behalf of the Foundation for Science and Technology, through the FUSION: R&I Research Excellence Programme. (Corresponding author: Hadi Naderiallaf).

Hadi Naderiallaf is with the Power Electronics, Machine and Control Group (PEMC), The University of Nottingham, Nottingham, U.K. (e-mail: Hadi.Naderiallaf@nottingham.ac.uk).

stress on the insulation between winding turns, resulting in a not negligible PD activity. To achieve a PD-free design, it is imperative to keep the voltage drop across turn-to-turn insulation below the minimum PDIV [2].

The most significant electrical stress, stemming from PD activity, primarily affects turn-to-turn insulation due to interactions between inverters and coil windings [3], [4]. Turn-to-turn insulation stands as the pivotal and vulnerable component within the electrical machine insulation system. PD emerges as the primary stress factor confronting this insulation. This matter becomes exceptionally critical when the electric field linked to this insulation surpasses the PD inception threshold, incepting PD activity and accelerating insulation deterioration. This concern escalates when winding wires are manufactured out of organic insulation, as PD can result in premature failure, potentially reducing the lifetime to a mere matter of days or even hours [5].

Environmental factors, like H and T , significantly influence the PDIV of turn-to-turn insulation. The impact of H on PDIV can exhibit varying decreasing or increasing trends across different T s, leading to inconsistent results. With no comprehensive model to predict PDIV based on H and comprehend its behaviour in varying H conditions, conducting time-consuming and expensive PDIV tests in controlled climate chambers remains imperative for reliable results. Unfortunately, these tests often produce conflicting outcomes due to the non-monotonic nature of PDIV concerning H . Additionally, there is currently no consensus on reporting PDIV results based on RH, AH, or both [6].

To address these gaps, this paper aims to expand the model proposed in [7], forecasting PDIV as a function of H across different T s. The model relies on the fitting parameter K , representing the natural logarithm of the critical electron count that defines the transition from Townsend to streamer discharges in the context of SCSIC. Previous SCSIC research, including [7], [8], [9], and [10], centred on modeling at a fixed H level. However, given the importance of motor insulation reliability under varying environmental conditions, this paper comprehensively explores PDIV modeling and PD phenomena across a broad range of T s and H levels to achieve a PD-free design. Another innovation in this paper is the introduction of a novel approach that utilizes SCSIC-derived SIPs: C_{FLL}, α_{eff} , E_{inc} , and V_{firing} , to investigate PD phenomena under fluctuating H conditions at varying T s. The paper demonstrates how these SIPs can be interpreted to deduce trends in PD charge amplitude and the damage caused by PD concerning H at different T s. Furthermore, the paper underscores instances where surface conductivity and η take precedence over other key parameters, such as ϵ_r , particularly when H levels change.

II. METHODOLOGY

To achieve these aims, the methodology involves a series of steps: (a) Measuring PDIV for turn-to-turn TPs under different T conditions, considering RH as a variable. Subsequently, (b) conducting electric field simulations and

calculating ionization swarm parameters under the B10 PDIV (i.e., 10% probability within the 2-parameter Weibull distribution) for each specific scenario (i.e., several RH and T s combinations). (c) Utilizing the SCSIC, N_c is determined, which represents the electron count threshold denoting the transition to streamer discharge under the B10 PDIV condition. (d) Next, deriving the fitting parameter K , represented as the natural logarithm of N_c , for each distinct case under the 10% probability. Given that K exhibits variations in response to RH at diverse T settings, (e) K equations are formulated as functions of RH at varying T s. (f) These derived K equations are employed to predict B10 PDIV. Finally, (g) the influence of H on SIPs is comprehensively analysed and explained across different T ranges.

To perform the PDIV modeling based on SCSIC, experimental data for PDIV is needed to derive K as a function of H at different T s. In the following, first, the used test samples for the PDIV measurements are introduced. Then, the PDIV measurement setup is described, and finally, the measurement conditions and procedure are explained.

A. Test Samples

PDIV measurements are conducted on TPs, mimicking the insulation system of random-wound electrical machines (Fig. 1). The cylindrical magnet wire insulation is grade II, comprising a THEIC-modified polyester-imide base and a polyamide-imide topcoat, both with a thermal class of 220°C. The insulated wire characteristics are listed in Table I. The method for measuring copper wire diameter, insulation thickness, and ϵ_r is detailed in [10]. To manufacture TPs, wires are twisted 12 times with a 7 N load tension, resulting in a 125 mm twisted section [12]. For each test condition (i.e., H and T combination), a dataset is compiled using five fresh TPs that have not been electrically stressed.

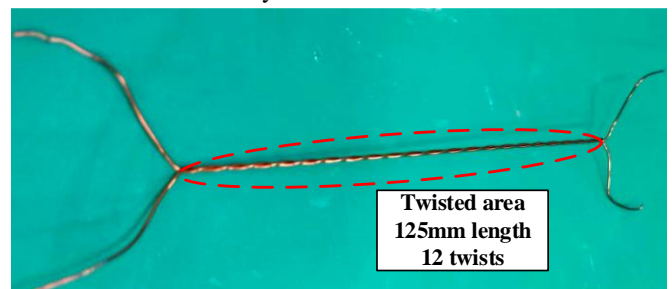


Fig. 1. A typical twisted pair used for PDIV tests.

TABLE I
INSULATED WIRE CHARACTERISTICS

Parameter	Value
Insulation grade	Grade II
Insulation basecoat	THEIC-modified polyester-imide
Insulation overcoat	Polyamide-imide
Thermal class	220°C
Bare copper wire diameter	0.556 mm
Insulation thickness	28.5 μm
Relative permittivity	4.31

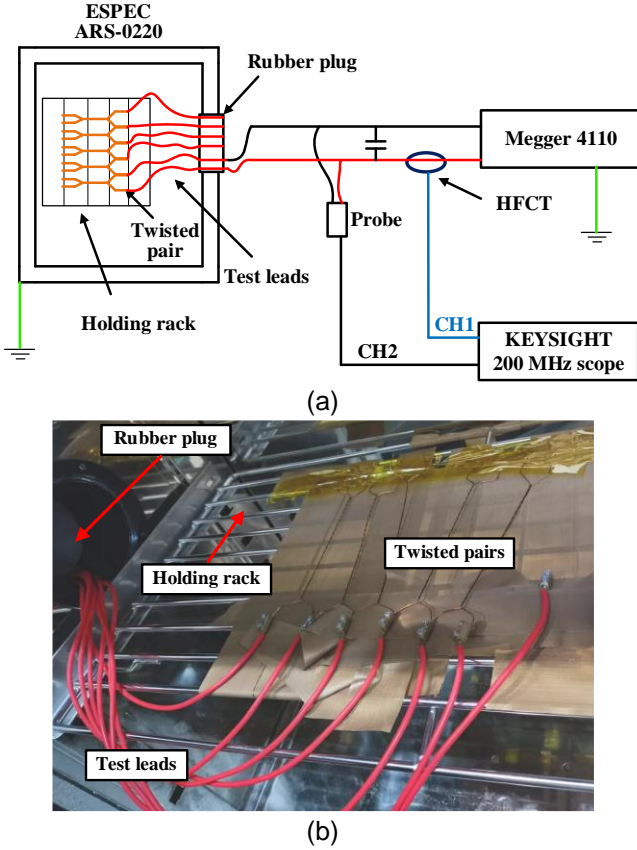


Fig. 2. (a) Diagram illustrating the setup and layout of PDIV testing and connections, and (b) specimens in the environmental chamber.

B. PDIV Test Setup

To assess the turn-to-turn insulation in inverter-fed motors, IEC 60034-18-41 [2] allows PDIV measurement under either sinusoidal or impulsive voltage excitations. When using a 50 Hz AC supply, it provides a cautious assessment for turn-to-turn insulation exposed to 2-level inverter or surge generator waveforms [13], [14], [15]. Notably, PDIV measured at 50 Hz AC excitation tends to be lower than that with steep-fronted square waveforms ($< 1 \mu\text{s}$ rise time) [16]. Hence, despite the waveform disparity between the turn-to-turn voltage and AC voltage, this study employs a 50 Hz sinusoidal waveform for AC PDIV tests to guarantee conservative PDIV values.

As shown in Fig. 2, PDIV tests are performed within an ESPEC ARS-0220 environmental chamber with a 0.22 m^3 test volume, offering precise T and H control. A rubber plug serves to guide test leads into the climate chamber while preventing external T and H from entering. The AC power source, the Megger 4110, produces AC 50 Hz voltage excitation. An HV differential probe (PICO® TA044) with a 70 MHz bandwidth, 1000:1 voltage attenuation ratio, and $10 \text{ M}\Omega$ impedance measures the voltage across the TP. Monitoring of the excitation voltage is done via a Keysight® DSOX2024A oscilloscope. For PD signal capture, a conventional indirect circuit is utilized. To enhance measurement sensitivity and improve the signal-to-noise ratio, a PD-free 4.7 nF coupling

capacitor is connected in parallel to the test TP. The PD sensor employed is a Kanggaote (KGT) HFCT with a bandwidth spanning from 0.3 to 100 MHz. The PD sensor is directly connected to the oscilloscope, with a PD detection threshold set at 1 mV.

C. Measurement Conditions and Test Procedure

PDIV tests are performed at eight RH levels: 20%, 30%, 40%, 50%, 60%, 70%, 80%, and 90%. The T remains constant at four distinct values: 25°C , 40°C , 60°C , and 90°C . However, it's important to mention that the climate chamber's limitations prevent achieving 20% RH at 25°C . Consequently, there are a total of 31 case studies, encompassing various combinations of RH and T settings. The control range of RH in the climate chamber for PDIV tests varies with temperature. For example, at 10°C , 20°C , and 30°C , the RH is adjustable within the ranges of 60%-98%, 30%-98%, and 20%-98%, respectively. Across the temperature span of 40°C to 95°C , the RH exhibits a broader adjustable range, extending from 10% to 98%.

Before commencing each PDIV test, sufficient time is allowed for the RH and T to stabilize. During the tests, the applied voltage peak is incrementally raised in 10 V steps. Additionally, because two prerequisites must be met for a PD to occur: (1) the electric field in the air wedge between the two wires surpasses the inception field, and (2) a free electron becomes available to initiate the avalanche, a 2-minute wait at each step is opted for to ensure precise PDIV measurements. Upon detecting PD, the peak voltage value at that moment is carefully noted as the PDIV. The dataset gathered from testing five pristine TPs is post-processed using a 2-parameter Weibull distribution, and the reported PDIV for each RH and T pair corresponds to the B10 value of this distribution. The insulation system reliability is often expressed by a selected percentile of the distribution tail [21], and a commonly adopted value represented by the B10, which corresponds to the non-exceeding probability in Weibull distributions fitting each data group. Therefore, the B10 of PDIV is selected as the reference value for expressing both PDIV test results and the PD model, although lower percentile values could have been chosen in case a more stringent reliability constraint was demanded.

III. PDIV MODELING THROUGH SCSIC

According to SCSIC [17], a Townsend avalanche transitions into a streamer when condition (1) is fulfilled:

$$K \leq \int_0^{x_c} \alpha_{\text{eff}}(x) \cdot dx \quad (1)$$

K is a dimensionless constant, denoting the natural logarithm of N_c , the critical number of electrons at the avalanche's head. When N_c is reached, it initiates the emergence of fast-moving filamentary streamers from the head of the avalanche, signifying the transition from Townsend to streamer discharge [18]. In (1), x represents the distance travelled by a single primary electron starting at the cathode, while x_c is the critical avalanche length along the electric FL. Beyond x_c , the

transition from Townsend to streamer discharge takes place, marking the onset of the earliest discharge event. Furthermore, α_{eff} , obtained from (2):

$$\alpha_{\text{eff}} = \alpha - \eta \quad (2)$$

Here, α and η depend on factors such as electric field intensity, air pressure or gas number density, T , and H [19]. In [11], it was demonstrated that $p \cdot d$ values below $100 \text{ mbar} \cdot \text{mm}$ apply to air wedges in turn-to-turn insulation systems, spanning from atmospheric pressure (1000 mbar) down to 100 mbar, with d representing air gap length and p air pressure. Unlike typical air discharges, adopting $K = 18.42$, equivalent to 10^8 electrons as proposed by [18], may result in an overestimation of avalanche breakdown when $p \cdot d$ is below $1 \text{ bar} \cdot \text{cm}$ [19]. In [7], a simplified FEM model calculates K for small air wedges and non-uniform field distribution in turn-to-turn insulation. The authors approximated $K \approx 6$ at atmospheric pressure (1000 mbar) considering temperature variations based on Schumann's streamer inception criterion [17]. However, there is a gap in the literature regarding variations in K for air with variable humidity levels.

PDIV measurements are performed on each pristine specimen only once. This approach is adopted to (a) avoid PDIV reduction caused by residual charges from previous PD activities [20], and (b) account for the potential PDIV reduction due to insulation damage resulting from PD activity, particularly considering the organic nature of the insulation material. For each tested ambient condition, covering different H and T combinations, five fresh samples are tested. To minimize potential influences from space charge accumulation on the electric field distribution within the air wedge and PDIV readings, bipolar excitations with polarity reversals (e.g., AC) are preferred for PDIV measurements over voltage waveforms with a DC component (e.g., unipolar excitations) [20], [21], [22]. Consequently, the initiation of a discharge event hinges exclusively on air ionization.

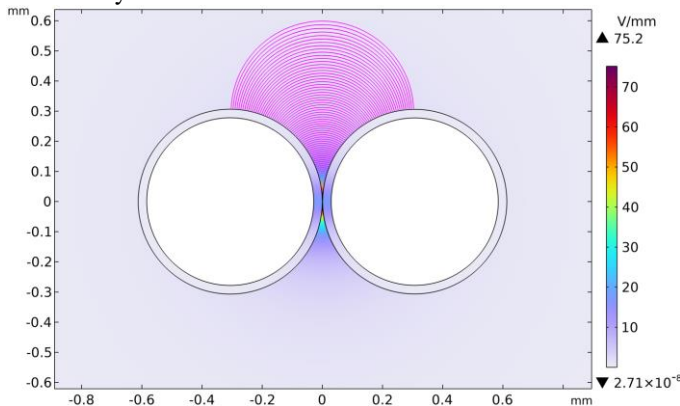


Fig. 3. Electric field distribution simulation between two cylindrical insulated wires in 2D COMSOL Multiphysics® [10].

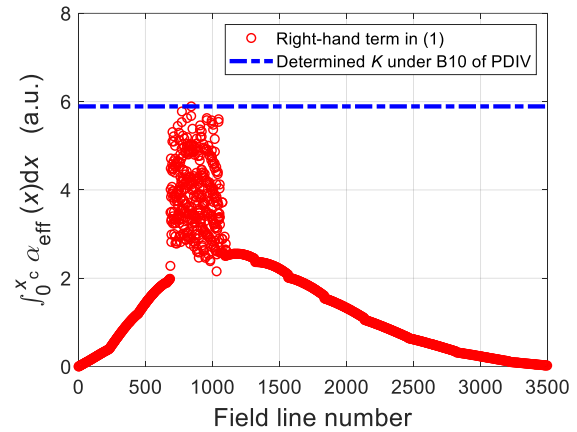


Fig. 4. Visualization of the K determination approach.

A. Determining Schumann Constant (K)

To determine K , the initial requirements involve: a) conducting electric field distribution simulations to derive FLLs in the air wedge and electric field intensity along each FL, and b) calculating α_{eff} as a function of electric field intensity. For detailed methods regarding the derivation of FLLs, electric field magnitude, and α_{eff} , refer to [9], [10], [11]. The algorithm outlined in [8], [9], [10] and [11] is developed and coded in MATLAB to determine the K value under B10 of PDIV across various H levels and T_s .

For brevity, the main steps in the calculation are listed below [9], [10] and [11]:

- 1) Import the reference database from FEM electrostatic computations at a unit voltage (i.e., 1 V), including FLLs vs. electric field intensity (see Fig. 3).
- 2) Update electric field magnitude along each FL using linearity for B10 of PDIV.
- 3) Calculate α_{eff} based on electric field intensity along each FL from step 2 using BOLSIG+ software [23], [24].
- 4) Calculate the right-hand term in (1) for all FLs within the air wedge formed between the two insulated wires.
- 5) Record the maximum value obtained at step 4 as the derived K corresponding to B10 of PDIV. This K value is used in the SCSIC to predict B10 of PDIV at different H and T_s (see Fig. 4).
- 6) Identify the FL yielding the highest K value as the reference, known as CFL. Use CFL to derive SIPs, including CFLL, as well as other parameters associated with CFL, such as α_{eff} , E_{inc} , and the V_{firing} [9], [10].

Fig. 4 depicts a CritR, occurring at a specified range of FL numbers, corresponding to specific electric field intensity levels. Within this region, α_{eff} and the right-hand term in (1) exhibit significant dispersion and growth [9], [10]. As a result, the maximum values of the right-hand term in (1), represented as K , consistently fall within this vital zone. This CritR plays a decisive role in determining both K and the computation of SCSIC-derived SIPs along the CFL.

B. Predicting PDIV via the Determined K

Expanding on the algorithm proposed in [7], the prediction of PDIV across various H and T levels is extended using SCSIC. Detailed information on this iterative approach can be found in [9], [10] and [11]. For brevity, the main steps are outlined below:

- 1) Choose a suitable K value tailored to the particular H and T conditions, aiming for the desired PDIV probability, such as B10.
- 2) Simulate the electric field distribution within the air wedge between the two insulated wires using a unit voltage (i.e., 1 V) to create a database containing FLLs and their corresponding electric field intensities (see Fig. 3).
- 3) Start by setting an initial PDIV value below the actual PDIV, such as 50 V.
- 4) Increase the electric field intensity along each FL in the imported database from step 2 using a linear approach.
- 5) Using the electric field strength computed in step 4, determine α_{eff} for each FL by referencing the BOLSIG+ software [23], [24].
- 6) With the selected K value from step 1, the computed FLLs from step 2, and the obtained α_{eff} from step 5, check if condition (1) is satisfied for at least one electric FL. If condition (1) is not met, increase the applied voltage (e.g., by 0.5 V) and return to step 4.
- 7) The iterative process concludes when condition (1) is satisfied for at least one FL. Once this condition is met, stop the iteration, and record the applied voltage as the predicted B10 of PDIV under the desired H and T conditions.

IV. RESULTS AND DISCUSSIONS

A. Measured PDIV

Fig. 5 illustrates a consistent trend across T s (25°C, 40°C, and 60°C): PDIV decreases as H levels (RH and AH) rise. This decline is likely due to increased α_{eff} at higher T s due to higher H , resulting in a lower PDIV triggering voltage. Another, less likely, explanation involves water molecules entering solid insulation, increasing its ϵ_r , and intensifying the electric field in the air gap, thereby reducing PDIV [25]. However, this explanation isn't applicable to our PDIV tests due to slow insulation water absorption, which contrasts with our relatively quick PDIV measurements. For example, immersing the polyamide-imide in water for 48 hours results in only a 4% water absorption by mass [26]. Furthermore, the increase in ϵ_r due to water absorption is less significant at higher T s like 60°C due to the lower ϵ_{rw} at elevated T s (e.g., ϵ_{rw} measures 78.3 at 25°C and 66.8 at 60°C) [28]. The reduction in the rate of PDIV decrease from 25°C to 60°C with increasing RH can be attributed to increased surface conductivity resulting from higher AH at constant RH at higher T s. This increased surface conductivity can reduce the electric field intensity in the air gap. However, at these T s, the influence of α_{eff} rising with increased RH outweighs the effect of increased surface conductivity, as evidenced by PDIV decreasing with higher RH. It's worth noting that the extent of PDIV reduction in response to

increased H at these T s can vary among wires, depending on the composition of the insulating material, which may react differently to changes in H [28]. In Fig. 5, a significant distinction stands out: unlike lower T s, at 90°C, PDIV increases with higher H . The most notable PDIV boost occurs between RH = 40% (AH = 169 g/m³) and RH = 50% (AH = 211.2 g/m³). Several factors contribute to this phenomenon. Firstly, as speculated in [28], elevated H at high T s, such as 90°C, marked by increased AH, promotes water molecules acting as electronegative gases. Consequently, η significantly increases near the enamel surface, where condensation is more probable, leading to a heightened PDIV. Specifically, increased η demands a higher applied voltage to enhance the electric field along the FL until the avalanche size reaches the critical point for discharge initiation. Secondly, at 90°C, rising H increases the presence of water molecules, enhancing surface conductivity, as demonstrated in [29]. As a result, the electric field within the air gap weakens, leading to a higher PDIV. Additionally, at 90°C, H increments lead to an increase in the $\tan\delta$ [30]. This implies greater losses for the applied voltage, possibly due to enhanced surface conductivity. Consequently, a higher voltage is required to induce PD in the air gap, as confirmed in [31]. In this context, at 90°C, higher H results in a higher PDIV, albeit with increased losses due to elevated H levels.

The ϵ_r of polyamide-imide remains stable within the range of 25°C to 90°C, as confirmed in [28]. Therefore, variations in PDIV due to T cannot be ascribed to ϵ_r alterations. As depicted in Fig. 5, under constant RH, rising T results in an increase in AH since the dew point shifts to higher T levels. Higher AH values generally correlate with increased α_{eff} , depending on the electric field (see later Fig. 7). Additionally, rising T decreases gas density and enhances the availability of initial electrons, influenced by a weaker surface work function through the Schottky-Richardson emission mechanism [10]. These factors collectively contribute to a PDIV reduction within a specific range of RH due to T elevation. For instance, across all constant RH values, a T increase from 25°C to 40°C leads to lower PDIV. As T rises, a lower range of RH exhibits reduced PDIV due to elevated T . For example, PDIV decreases as T rises from 25°C to 60°C at RH \leq 40%, and PDIV diminishes as T increases from 25°C to 90°C at RH \leq 30%. Indeed, at RH levels of 20% and 30%, elevating the temperature from 25°C to 90°C results in a drop in gas number density, thereby increasing the mean free paths for collisions between free electrons and gas-neutral molecules. This extended path allows electrons to be accelerated over greater distances, acquiring more kinetic energy. Thus, under the same voltage, the number of ionization events per unit length increases [10]. This effect prevails over the impact of higher AH caused by the temperature increase at constant RH (i.e., 20% and 30%). Consequently, lower voltages are needed to initiate PD. This suggests that at higher T s, the overall trend of PDIV reduction occurs at lower H levels. Indeed, at elevated T s (e.g., 60°C and 90°C), when RH surpasses a certain threshold, the impact of AH on PDIV becomes more significant than the effect of T on PDIV drop.

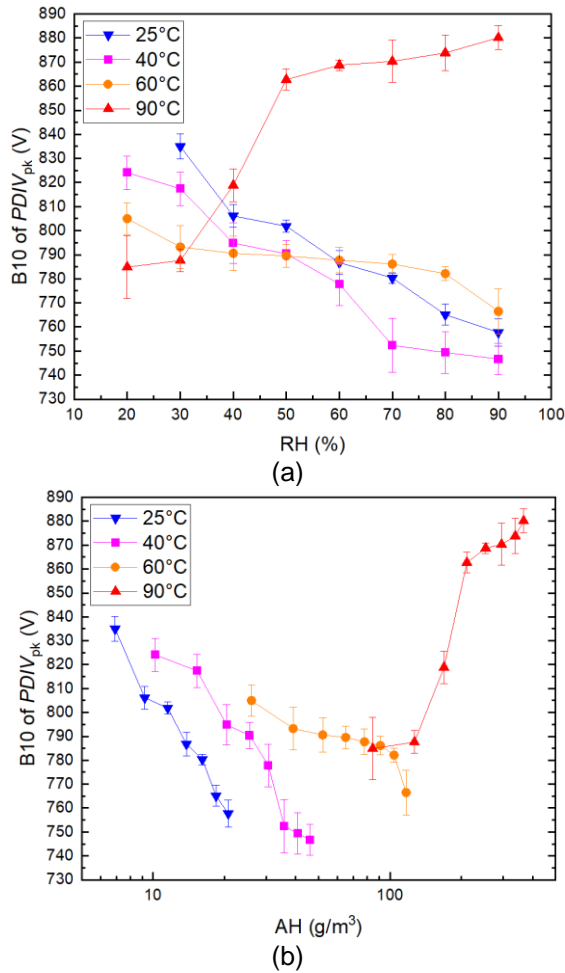


Fig 5. B10 of PDIV peak measured at different T s as a function of (a) RH and (b) AH. Confidence intervals with a probability of 95% are also shown.

Consequently, PDIV does not decrease with rising T . For instance, at 90°C, for ($RH \geq 40\%$ or $AH \geq 169 \text{ g/m}^3$), PDIV exceeds that at lower T s. Similarly, at 60°C, for ($RH \geq 70\%$ or $AH \geq 78.04 \text{ g/m}^3$), PDIV surpasses that at 25°C and 40°C. This enhanced PDIV can be attributed to increased surface conductivity and elevated η . Surface conductivity benefits from both higher T and AH at constant RH, while η , driven by increased AH [28], necessitates a higher applied voltage to amplify the electric field along the FL. As a result, an avalanche can reach its critical size and initiate a discharge event at a higher applied voltage (i.e., higher PDIV). In summary, T impact on PDIV depends on the H level, influenced by the interplay of multiple factors, including gas density, surface conductivity, and η . In Fig. 5, across various case studies with different combinations of H and T , the minimum and maximum PDIV values are evident when RH is set at 90%. The lowest PDIV occurs at 40°C ($AH = 46 \text{ g/m}^3$), measuring 746.7 V, while the highest PDIV registers at 90°C ($AH = 366.3 \text{ g/m}^3$), reaching 880.13 V. Surprisingly, at $RH = 90\%$, despite the 87.44% reduction in AH when the T drops from 90°C to 40°C, the PDIV decreases by 15.16%.

B. Schumann Constant (K)

Fig. 6 reveals how H affects K at various T s. At 25°C, 40°C, and 60°C, an elevation in H (both RH and AH) leads to a decline in K . However, this reduction becomes less pronounced as the temperature increases from 25°C to 60°C. In other words, the sensitivity of K to H variations diminishes as the T rises from 25°C to 60°C. At 90°C, higher H generally increases K , except when shifting from $RH = 40\%$ to $RH = 50\%$. The rate of K increase at 90°C becomes steadier from $RH = 50\%$ onward. Regarding T impact on K , Fig. 6 shows that when $RH \leq 40\%$, K increases as T goes from 25°C to 90°C. A similar trend occurs for $RH = 50\%$ to $RH = 90\%$, except at 90°C, where K rises from 25°C to 60°C. Fig. 6 highlights the maximum and minimum K values observed at 90°C, occurring at $RH = 40\%$ (or $AH = 169 \text{ g/m}^3$) and $RH = 50\%$ (or $AH = 211.2 \text{ g/m}^3$), respectively. Notably, a sharp K reduction occurs as H shifts from $RH = 40\%$ to $RH = 50\%$.

To scrutinize the sudden K reduction at 90°C, the right-hand term of (1) is graphed across all FL numbers, as depicted in Fig. 7. This figure sequentially labels FLs from shortest to longest, denoting higher electric field strength for shorter FLs and lower strength for longer FLs.

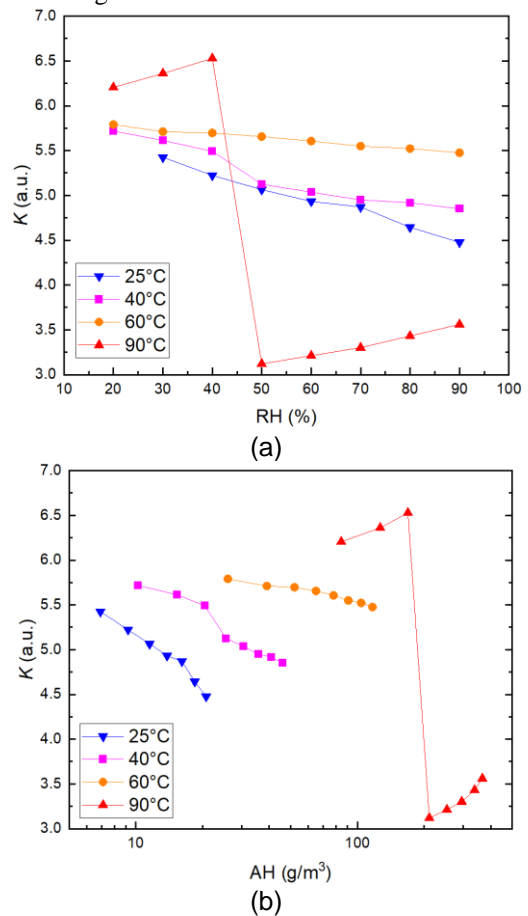


Fig 6. Derived K under B10 of PDIV peak at different T s as a function of (a) RH and (b) AH.

In Fig. 7, a CritR materializes, characterized by a significant increase in α_{eff} . This region exerts a pivotal influence on K by establishing its maximum value. The CritR thins as RH

escalates from 20% to 40% and completely vanishes at RH = 50%. Consequently, K undergoes a pronounced decline at 90°C and RH = 50%. Additionally, Fig. 7 illustrates that α_{eff} tends to increase with higher H levels across the various FLLs.

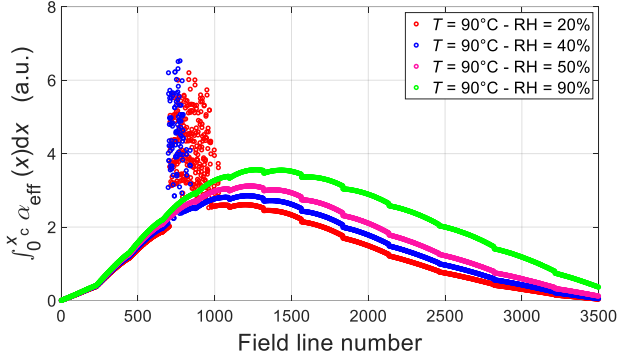


Fig 7. Disappearing of the CritR of α_{eff} at 90°C and RH \geq 50%.

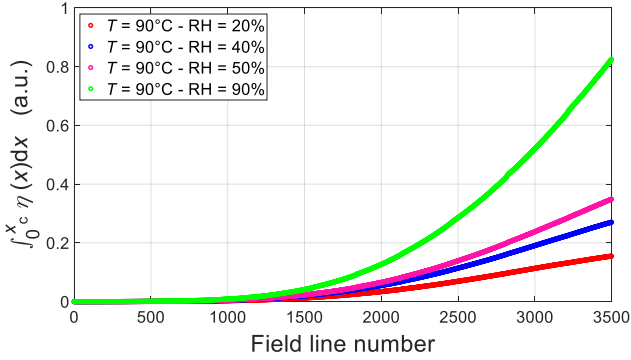


Fig 8. Increase of η with RH at 90°C across different FLs.

This humidity-induced impact on α_{eff} is less noticeable in shorter FLs characterized by stronger electric field intensities [10]. To uncover the cause behind the vanishing of this CritR, the integral of η across individual FLs is calculated and illustrated in Fig. 8. The FLs in Fig. 8 mirror those in Fig. 7, sharing the same ordering from shortest to longest, representing varying electric field strengths. Fig. 8 demonstrates that at 90°C, the integral of η rises with increasing H , as speculated in [28]. However, within the CritR (encompassing FL numbers 500 to 1000), this integral remains nearly constant across varying RH values. This suggests that the increase in η due to H rise is closely linked to the intensity of the electric field, with its effects becoming more pronounced when considering longer FLs where the electric field strength is weaker. Therefore, the primary factor behind the CritR's disappearance and the ensuing sharp K reduction is not the η increase, but rather a substantial α decrease in (2) at 90°C and RH = 50%. This also explains the substantial increase in PDIV at 90°C when transitioning from RH = 40% to RH = 50%, as seen in Fig. 5. At 90°C, the disappearance of CritR in α_{eff} between RH 40% and 50% signifies a transition. Initially, CritR shows a substantial α_{eff} increase within a specific electric field range. In the driest air (RH = 20%), this occurs from 4.4 to 6.7 kV/mm, with the peak at 5.7 kV/mm (α_{eff} : 271.6 mm⁻¹). At RH 40%, CritR narrows (5.9 to 7 kV/mm), peaking at 6.4 kV/mm (α_{eff} : 323.3 mm⁻¹).

At RH 50%, CritR vanishes, at this point, no significant α_{eff} surge exists; instead, α_{eff} steadily rises with electric field intensity (Fig. 7). Consequently, the transition from RH 40% to 50% sees α_{eff} decrease notably from 323.3 mm⁻¹ to 65.7 mm⁻¹, about fivefold.

To enhance PDIV prediction accuracy concerning H based on SCSIC, precise K values are essential. Linear regression models are employed, using the least squares method to fit K values obtained from Fig. 6. These models represent K as an RH-dependent function at various T s listed in Table II. Calculated slopes reveal a 71.1% reduction in the K reduction rate from 25°C to 60°C concerning RH. Furthermore, the K increasing rate at 90°C decreased by 32% when transitioning from (20% \leq RH < 40%) to (50% \leq RH \leq 90%).

It is essential to note that the derived K equations are established with certain initial assumptions, which involve overlooking variations in ϵ_r , surface conductivity, surface work function, and initial electron generation probability within solid insulation concerning T and H fluctuations. However, real measured PDIV values are employed to derive these K values.

TABLE II
FITTED LINEAR REGRESSION TO THE DERIVED K AT
DIFFERENT T AND RH VALUES FROM FIG. 6.

T	RH	$K_{(RH)}$
25°C	30% \leq RH \leq 90%	$-1.50 \cdot RH + 5.85$
40°C	20% \leq RH \leq 90%	$-1.34 \cdot RH + 5.95$
60°C	20% \leq RH \leq 90%	$-0.43 \cdot RH + 5.86$
90°C	20% \leq RH < 40%	$1.62 \cdot RH + 5.88$
	40% \leq RH < 50%	$-34.08 \cdot RH + 20.16$
	50% \leq RH \leq 90%	$1.10 \cdot RH + 2.55$

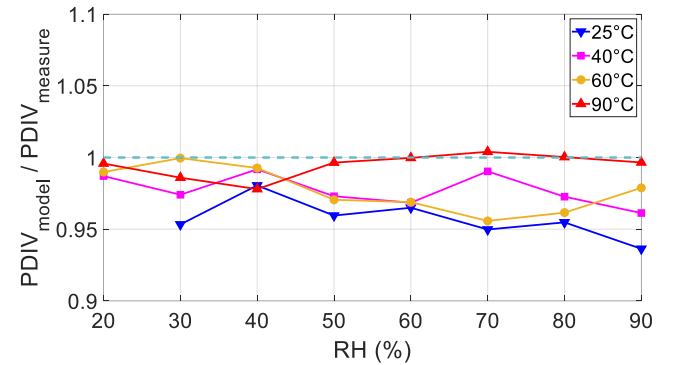


Fig. 9. The ratio of modelled and measured B10 of PDIV peak as a function of RH for different T s.

TABLE III
PDIV PREDICTION ERROR IN (%)

RH (%)	20	30	40	50	60	70	80	90
25°C	-	-4.66	-1.95	-4.05	-3.5	-5.02	-4.52	-6.36
40°C	-1.29	-2.59	-0.82	-2.7	-3.15	-0.96	-2.73	-3.87
60°C	-1.01	-0.04	-0.73	-2.94	-3.11	-4.42	-3.84	-2.11
90°C	-0.42	-1.41	-2.2	-0.35	-0.02	0.4	0.03	-0.34

Indeed, the objective is to obtain empirical fitting equations for K under simplified conditions to predict PDIV with the utmost accuracy and simplicity, avoiding the complexity of multiphysics phenomena.

C. PDIV Prediction Based on SCSIC

Using the equations in Table II and the PDIV prediction algorithm described in [9] and [10], the B10 of the PDIV peak is forecasted. Fig. 9 illustrates the ratio of modelled PDIV to measured PDIV, while Table III reports the PDIV prediction error in percentage.

Fig. 9 and Table III confirm that the derived K equations significantly improve the PDIV prediction accuracy, consistently exceeding 93.6% across various H and T combinations. The highest error, occurring at 25°C and RH = 90%, is 6.36%. These findings highlight the K equations' success in enhancing the PDIV prediction model rooted in SCSIC, providing valuable support for the PD-free design of inverter-fed motors.

Comparing PDIV prediction errors at constant RH values from 25°C to 90°C reveals that the highest accuracy occurs at 90°C, specifically between RH = 50% and RH = 90%. This improved accuracy can be attributed to the elimination of the CritR in α_{eff} , which occurs at RH = 50% onwards, as depicted in Fig. 7, due to the reduced dispersion of α_{eff} in this range. Additionally, the best PDIV prediction accuracy is achieved at high T s, specifically 90°C, with the highest prediction error, 2.2%, occurring at RH = 40%. This reaffirms the effectiveness of the derived linear regression equations in boosting accuracy across different RH levels.

D. CFLL

Fig. 10 shows how CFLL changes with RH at various T s. At 25°C, 40°C, and 60°C, CFLL decreases as RH increases, similar to the trend observed with K . However, at 90°C, CFLL reduces until RH reaches $\leq 40\%$, after which the CritR disappears (Fig. 7). Notably, at 90°C, a shift from RH = 40% to RH = 50% leads to a sharp CFLL increase, unlike K (see Fig. 6).

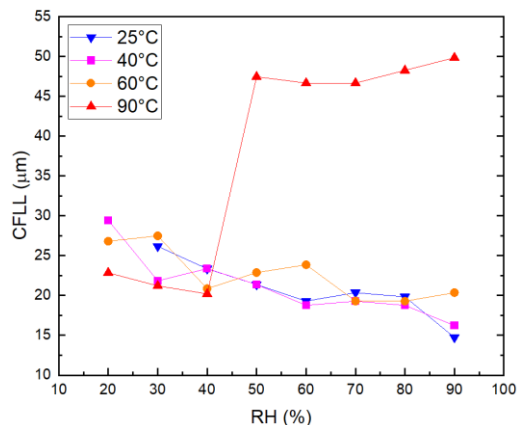


Fig. 10. CFLL as a function of RH for different T s.

At RH = 90%, higher T s extend CFLL, peaking at 90°C, where CFLL becomes 3.38 times longer compared to 25°C. Conversely, at the lowest H (RH = 20%), lower T s result in slightly longer CFLL. For instance, reducing the T from 90°C to 40°C increases CFLL by 1.29 times. Longer CFLL enables electrons in an avalanche to travel further, gaining more kinetic

energy. Consequently, under PDIV, PD activity becomes more damaging to insulation [11]. The most significant insulation damage due to PD occurs at maximum H and T (90°C and RH = 90%). This finding is corroborated by the shortest lifetime observed at RH = 90% in [32]. Additionally, at 90°C, the rapid CFL increase when transitioning from RH = 40% to RH = 50% suggests significantly more harm to insulation. Therefore, at 90°C, the insulation lifetime may be considerably shorter with PD activity at RH = 50% compared to RH = 40%, with the shortest lifetime occurring at RH = 90%. It's important to note that at 25°C, 40°C, and 60°C, CFL decreases with higher H , while PDIV decreases (see Fig. 5), and the dielectric loss factor ($\tan\delta$) increases [30].

E. Effective Ionization Coefficient

Fig. 11 displays how α_{eff} changes with RH across CFLL at various T s. Unlike CFLL, α_{eff} generally rises with increasing RH at 25°C, 40°C, and 60°C, explaining the declining PDIV at these T s (Fig. 5).

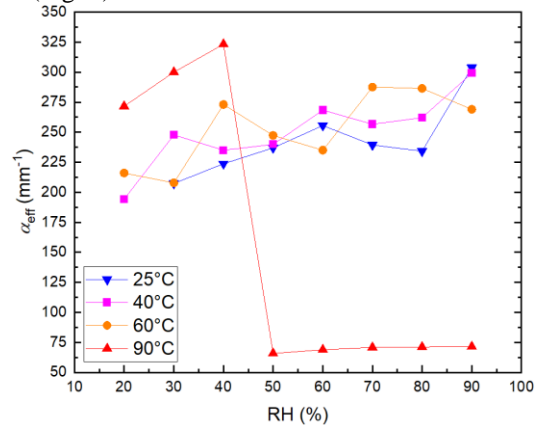


Fig. 11. α_{eff} as a function of RH for different T s.

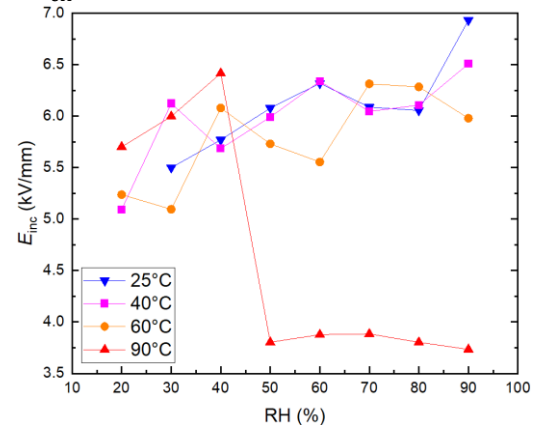


Fig. 12. E_{inc} as a function of RH for different T s.

At 90°C, α_{eff} mirrors K , indicating a direct relationship. The sudden α_{eff} drop from 40% to 50% RH is due to the CritR vanishing, causing a substantial PDIV increase at 90°C (Fig. 5). At extreme H levels (RH = 90% and RH = 20%), the T has opposite effects on α_{eff} compared to CFLL. At RH = 90%, higher T reduces α_{eff} due to η increase, leading to maximum PDIV at 90°C (Fig. 5) [28]. Conversely, at RH = 20%, higher T

elevates α_{eff} due to α increase, resulting in minimum PDIV at 90°C (Fig. 5). In summary, T increases η at high RH and α at low RH.

F. PD Inception Field

Fig. 12 illustrates the variation in the electric field across the CFL (i.e., E_{inc}) with changing RH at different T s. Notably, α_{eff} (Fig. 11) mirrors the E_{inc} trend in Fig. 12. At 25°C, 40°C, and 60°C, E_{inc} shows fluctuations with increasing RH. However, a comparison between the lowest RH and RH = 90% reveals that E_{inc} is higher at RH = 90%, aligning with the lower PDIV values depicted in Fig. 5. It is worth noting that the finite element simulation does not account for the increase in relative permittivity and surface conductivity of the solid insulation at RH = 90%. While the former can elevate E_{inc} , the latter can decrease it at RH = 90%. Despite these factors, at 25°C, 40°C, and 60°C, the higher E_{inc} at 90% can be attributed to a shorter CFL (Fig. 10).

At 90°C, E_{inc} follows a similar increasing trend to PDIV as RH transitions from 20% to 40%. This similarity arises from the unaccounted reduction in the simulated electric field due to surface conductivity, leading to a compensatory increase in computed E_{inc} . However, at 90°C, as PDIV increases from RH 50% to RH 90%, E_{inc} only experiences a slight increase up to RH 70%. Beyond this point, the electric field across CFL and PDIV demonstrate their typical inverse relationship. This observation suggests that the influence of surface conductivity is not predominant in this T and H range (i.e., $T = 90^\circ\text{C}$ and $\text{RH} \geq 70\%$).

Fig. 12 also demonstrates that T impact on E_{inc} resembles α_{eff} and opposes CFL at the highest and lowest H levels (RH 90% and RH 20%). For example, at RH 90%, increasing the T reduces E_{inc} , resulting in the highest PDIV at 90°C. Conversely, at RH 20%, higher T boosts E_{inc} , causing PDIV to decrease. Notably, at 90°C, transitioning from RH 40% to RH 50% leads to a significant drop in E_{inc} , correlating with PDIV's sharp increase in the same RH range (Fig. 5).

G. Firing Voltage

Fig. 13 illustrates the relationship between V_{firing} across the CFL under PDIV as a function of RH at various T s. V_{firing} correlates linearly with PD charge amplitude, [9], and PD-induced insulation damage [33], indicating greater insulation damage with higher V_{firing} . Moreover, V_{firing} aligns with CFL trends with respect to RH levels, reinforcing the connection between CFL and PD-related damage, as previously discussed in relation to Fig. 10.

Increased PD charge magnitude results in more electrons, leading to greater damage over time, especially when both electron count and energy increase. Electrons gain more kinetic energy when traversing a longer CFL, increasing the likelihood of exceeding the bond energies of insulation materials (typically 3-4 eV for Carbon-Carbon and Carbon-Hydrogen bonds). Excessive electron energy can cause erosion through DEA [34]. As a result, maximum damage occurs when

both V_{firing} and CFL reach their peaks, as observed at 90°C and RH = 90% in Figs. 13 and 10, even though PDIV is highest under these conditions. This finding aligns with the shortest lifetime observed at RH = 90% in [32].

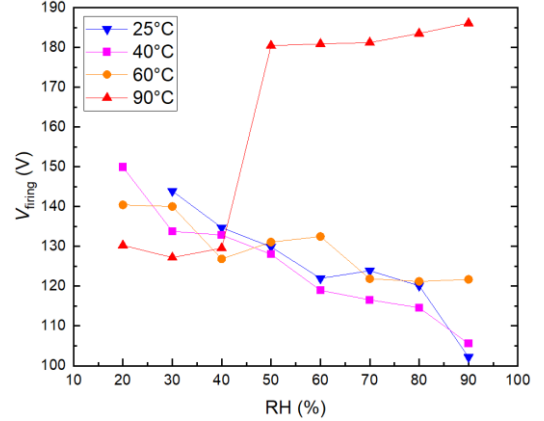


Fig. 13. V_{firing} as a function of RH for different T s.

Furthermore, at RH = 90%, increasing the T from 25°C to 90°C increases the V_{firing} by 1.82 times, indicating the potential for larger PD charge amplitudes and associated harm at higher T s and the highest H level. At 25°C, 40°C, and 60°C, V_{firing} decreases with increasing RH, implying a corresponding reduction in PD charge amplitude, in line with findings from [28], [32]. At 90°C, the transition from RH = 40% to RH = 50% is followed by a sharp rise in V_{firing} (Fig. 13) and CFL (Fig. 10), implying more damage and a shorter lifetime in the presence of PD at RH = 50% compared to RH = 40%.

V. CONCLUSION

This contribution emphasizes the humidity-dependent nature of K , a crucial factor for modeling PDIV based on SCSIC. By establishing equations for K in relation to H , PDIV predictions for inverter-fed motor turn-to-turn insulation with an accuracy exceeding 93.6% are achieved. Moreover, the research introduces a novel approach to understanding PD phenomena using SCSIC-derived SIPs.

Summarizing the main findings, at lower T s (e.g., 25°C, 40°C, and 60°C), increasing H results in reduced PDIV, K , CFL, and V_{firing} , while α_{eff} and E_{inc} increase. This consistent relationship between PDIV and E_{inc} underscores the reliability of the PD model, indicating that increased α_{eff} with rising H is the primary reason for reduced PDIV, with surface conductivity having a minor influence. At these lower T s, higher H levels lead to decreased V_{firing} and CFL, suggesting reduced PD charge amplitude and discharge energy, along with higher losses. However, a distinct trend emerges at higher T s (e.g., 90°C). Within the wide range of H levels considered, PD behaviour undergoes a transition phase from RH = 40% to RH = 50%. During this transition, PD behaviour shifts markedly, leading to a sharp increase in PDIV. This increase is attributed to the disappearance of a CritR of α_{eff} corresponding to a specific electric field range, resulting in a significant drop in K , α_{eff} , and E_{inc} . Additionally, higher V_{firing} and CFL values indicate increased PD charge magnitude and discharge energy,

translating to greater damage from PD activity under these conditions. In essence, the increase in PDIV at 90°C with rising H is accompanied by more harmful PD activity and increased losses. The direct relationship between E_{inc} and PDIV at $RH \leq 40\%$ is due to the dominant role of surface conductivity, while at $RH \geq 70\%$, the influence of η on PD behaviour becomes more pronounced. In conclusion, the predictive model for PDIV developed in this study provides valuable support for electrical machine insulation designers, facilitating precise PDIV predictions across varying H conditions. Moreover, the findings concerning SCSIC-derived SIPs shed light on the influence of H on turn-to-turn insulation PD behaviour, contributing to a deeper understanding of this phenomenon. As a future research step, the developed PD model will expand by including the impact of air pressure in varying humidity environments, to mirror the ambient conditions typical of aerospace applications.

REFERENCES

- [1] J.H. Williams, A. DeBenedictis, R. Ghanadan, A. Mahone, J. Moore, W.R. Morrow III, S. Price, and M.S. Torn, "The technology path to deep greenhouse gas emissions cuts by 2050: the pivotal role of electricity" *Science*, vol. 335, no. 6064, pp. 53-59, 2012.
- [2] IEC Std. 60034-18-41, "Rotating electrical machines - part 18-41: partial discharge free electrical insulation systems (Type I) used in rotating electrical machines fed from voltage converters - qualification and quality control tests," 2019.
- [3] E. Persson, "Transient effects in application of PWM inverters to induction motors," in *Proc. Conf. Rec. Annu. Pulp Paper Ind. Tech. Conf.*, Jun. 1991, pp. 228-233.
- [4] M. Melfi, A. M. J. Sung, S. Bell, and G. L. Skibinski, "Effect of surge voltage risetime on the insulation of low-voltage machines fed by PWM converters," *IEEE Trans. Ind. Appl.*, vol. 34, no. 4, pp. 766-775, Jul. 1998.
- [5] A. Cavallini, D. Fabiani, and G. C. Montanari, "Power electronics and electrical insulation systems - part 2: life modeling for insulation design," *IEEE Electr. Insul. Mag.*, vol. 26, no. 4, pp. 33-39, Jul-Aug. 2010.
- [6] M. Fenger and G. C. Stone, "Investigations into the effect of humidity on stator winding partial discharges," *IEEE Trans. Electr. Insul.*, vol. 12, no. 2, pp. 341-346, April 2005.
- [7] L. Lusuardi, A. Cavallini, M. G. de la Calle, J. M. Martínez-Tarifa, and G. Robles, "Insulation design of low voltage electrical motors fed by PWM inverters," *IEEE Electr. Insul. Mag.*, vol. 35, no. 3, pp. 7-15, May-Jun. 2019.
- [8] J. Gao, A. Rumi, Y. He and A. Cavallini, "Towards a holistic approach to inverter-fed machine design: FEM-based PDIV prediction of complete windings," *IEEE Trans. Electr. Insul.*, pp. 1-9, June 2023.
- [9] H. Naderiallaf, M. Degano, C. Gerada, "PDIV modeling for rectangular wire turn-to-turn insulation of inverter-fed motors through thermal ageing," *IEEE Trans. Electr. Insul.*, pp. 1-10, Aug. 2023.
- [10] H. Naderiallaf, Y. Ji, P. Giangrande, and M. Galea, "Temperature impact on PDIV for turn-to-turn insulation of inverter-fed motors: from ground level to cruising altitude," *IEEE Trans. Electr. Insul.*, pp. 1-10, Sep. 2023.
- [11] H. Naderiallaf, Y. Ji, P. Giangrande, and M. Galea, "Air pressure impact on the avalanche size for turn-to-turn insulation of inverter-fed motors," *IEEE Trans. Electr. Insul.*, pp. 1-10, Oct. 2023.
- [12] *Winding Wires - Test Methods - Part 5: Electrical Properties*, IEC Std. 60851-5, 2008.
- [13] A. Rumi, L. Lusuardi, A. Cavallini, M. Pastura, D. Barater, and S. Nuzzo, "Partial Discharges in Electrical Machines for the More Electrical Aircraft. Part III: Preventing Partial Discharges," *IEEE Access*, vol. 9, pp. 30113-30123, 2021.
- [14] A. Rumi, J. G. Marinelli, A. Cavallini, and P. Seri, "Can corona resistant wires ensure reliability in aerospace machine insulation?," in *2022 IEEE Electrical Insulation Conference (EIC)*, Knoxville, TN, USA, 2022, pp. 309-312.
- [15] G. C. Montanari and P. Seri, "About the definition of PDIV and RPDIV in designing insulation systems for rotating machines controlled by inverters," in *2018 IEEE Electrical Insulation Conference (EIC)*, 2018, pp. 554-557.
- [16] C. Abadie, "On-line non-intrusive partial discharge detection in aeronautical systems," Ph.D. dissertation, University of Toulouse, 2017.
- [17] W. O. Schumann, "Über das Minimum der Durchbruchfeldstärke bei Kugelelektroden," *Arch. Elektrotech. (Berl.)*, vol. 12, pp. 593-608, 1923 (in German).
- [18] H. Raether, "Electron avalanches and breakdown in gases," *Butterworth and Co. Publishers Ltd.*, 1964.
- [19] N. H. Malik, "Streamer breakdown criterion for compressed gases," *IEEE Trans. Electr. Insul.*, vol. EI-16, no. 5, pp. 463-467, Oct. 1981.
- [20] H. Naderiallaf, P. Giangrande, and M. Galea, "Characterization of PDIV, PDEV, and RPDIV in insulated wires under unipolar repetitive square wave excitations for inverter-fed motors," *IEEE Access*, vol. 11, pp. 51047-51063, 2023.
- [21] H. Naderiallaf, P. Giangrande and M. Galea, "Experimental considerations on the possible impact of space charge accumulation on partial discharges activity for wire insulations," in *2022 IEEE 4th International Conference on Dielectrics (ICD)*, Palermo, Italy, 2022, pp. 82-85.
- [22] H. Naderiallaf, P. Giangrande and M. Galea, "Impact of unipolar repetitive square wave voltage rise time and frequency on (RPDIV-PDIV) and (PDIV-PDEV)," in *2023 INSUCON - 14th International Electrical Insulation Conference (INSUCON)*, Birmingham, United Kingdom, 2023, pp. 236-240.
- [23] G. J. M. Hagelaar and L. C. Pitchford, "Solving the Boltzmann equation to obtain electron transport coefficients and rate coefficients for fluid models," *Plasma Sources Sci. Technol.*, vol. 14, no. 4, pp. 722-733, 2005.
- [24] "BOLSIG+ | Electron Boltzmann equation solver." [Online]. Available: <http://www.bolsig.laplace.univ-tlse.fr/>. [Accessed: Mar. 20, 2023].
- [25] M. Kaufhold, G. Borner, M. Eberhardt, and J. Speck, "Failure mechanism of the interturn insulation of low voltage electric machines fed by pulse-controlled inverters," *IEEE Electr. Insul. Mag.*, vol. 12, no. 5, pp. 9-16, Sept.-Oct. 1996.
- [26] L. Lusuardi, "Towards a partial discharge free insulation system for the More Electrical Transportation," Ph.D. dissertation, University of Bologna, Bologna, Italy, Mar. 2020.
- [27] C.G. Malmberg and A.A. Maryott, "Dielectric constant of water from 0° to 100°C" *Journal of research of the National Bureau of Standards*, vol. 56, no. 1, pp.1-8, 1956.
- [28] Y. Kikuchi *et al.*, "Effects of ambient humidity and temperature on partial discharge characteristics of conventional and nanocomposite enameled magnet wires," *IEEE Trans. Electr. Insul.*, vol. 15, no. 6, pp. 1617-1625, Dec. 2008.
- [29] T. Wakimoto, H. Kojima, and N. Hayakawa, "Measurement and evaluation of partial discharge inception voltage for enameled rectangular wires under AC voltage," *IEEE Trans. Electr. Insul.*, vol. 23, no. 6, pp. 3566-3574, Dec. 2016.
- [30] Y. Ji *et al.*, "Partial discharge investigation under humidity conditions via dissipation factor and insulation capacitance tip-up test," *IEEE Trans. Electr. Insul.*, vol. 29, no. 4, pp. 1483-1490, Aug. 2022.
- [31] H. Naderiallaf, M. Degano, and C. Gerada, "Assessment of edgewise insulated wire bend radius impact on dielectric properties of turn-to-turn insulation through thermal ageing," *IEEE Trans. Electr. Insul.*, pp. 1-10, Aug. 2023.
- [32] P. Wang, Y. Li, A. Cavallini, J. Zhang, E. Xiang, and K. Wang, "The influence of relative humidity on partial discharge and endurance features under short repetitive impulsive voltages," in *2018 IEEE Conference on Electrical Insulation and Dielectric Phenomena (CEIDP)*, Cancun, Mexico, 2018, pp. 506-509.
- [33] H. Naderiallaf, P. Seri and G. C. Montanari, "Effect of voltage slew rate on partial discharge phenomenology during voltage transient in HVDC insulation: the case of polymeric cables," *IEEE Trans. Electr. Insul.*, vol. 29, no. 1, pp. 215-222, Feb. 2022.
- [34] A. Rumi, J. G. Marinelli, P. Seri, M. Kohler, and A. Cavallini, "Performance of corona resistant insulation for aerospace," in *2021 IEEE Electrical Insulation Conference (EIC)*, Denver, CO, USA, 2021, pp. 22-25.